

## Frequency dependence of pulsar radiation patterns

J. Gil<sup>1</sup>, Y. Gupta<sup>2</sup>, P.B. Gothoskar<sup>2,3</sup> and J. Kijak<sup>1</sup>

jag@astro.ca.wsp.zgora.pl

Received \_\_\_\_\_; accepted \_\_\_\_\_

---

<sup>1</sup>Institute of Astronomy, Zielona Góra University, Lubuska 2, 65-265, Zielona Góra, Poland

<sup>2</sup>National Centre for Radio Astrophysics, TIFR, Pune University Campus, Pune 411 007, India

<sup>3</sup>Present Address : Veritas Software India Pvt. Ltd., Pune 411020, India

## ABSTRACT

We report on new results from simultaneous, dual frequency, single pulse observations of PSR B0329+54 using the Giant Metrewave Radio Telescope. We find that the longitude separation of subpulses at two different frequencies (238 and 612 MHz) is less than that for the corresponding components in the average profile. A similar behaviour has been noticed before in a number of pulsars. We argue that subpulses are emitted within narrow flux tubes of the dipolar field lines and that the mean pulsar beam has a conal structure. In such a model the longitudes of profile components are determined by the intersection of the line of sight trajectory with the frequency-dependent cones of maximum mean intensity, while the longitudes of subpulses are determined by the intersection of the line of sight trajectory with subpulse-associated emission beams. Thus, we show that the difference in the frequency dependence of subpulse and profile component longitudes is a natural property of the conal model of pulsar emission beam. We support our conclusions by numerical modelling of pulsar emission, using the known parameters for this pulsar, which produce results that agree very well with our dual frequency observations.

*Subject headings:* pulsar: subpulses: mean profiles:

## 1. Introduction

It is generally believed that the frequency dependence of pulsar radiation patterns (subpulses, profile components etc.) reveals the so called radius-to-frequency mapping effect :  $r(\nu) \propto \nu^{-p}$ , where  $r$  is the emission altitude corresponding to the frequency  $\nu$  and  $p$  is a positive exponent. The coherent radio emission from pulsars must be generated

due to some instability occurring within the stream of relativistic plasma flowing along dipolar field lines (e.g. Kazbegi et al. 1996; Asseo & Melikidze 1998; Melikidze et al. 2000). It is commonly assumed that the emission process is narrow-band, that is, at a given radio emission altitude  $r$  a relatively narrow band of frequencies,  $\Delta\nu$ , centered at a certain  $\nu$  ( $\gg \Delta\nu$ ) is generated (Cordes 1978, 1992; Kijak & Gil 1998). As a result of the radius-to-frequency mapping and the diverging nature of dipolar field lines, the longitudes of details of the observed emission (such as peaks of subpulses and profile components, profile edges etc.) vary with frequency. The simplest result of this is the observation that the overall pulse width is usually broader at lower frequencies. One should realize that the actual radius-to-frequency mapping can be revealed only if the radiation processes can be traced along approximately the same dipolar field line (or narrow bundle of adjacent field lines). For this, one has to locate a narrow feature in the radiation pattern (pulse window), which is apparently correlated in terms of intensity at different observing frequencies. The frequency dependence of the longitude of occurrence of such correlated emission features is given by  $\varphi(\nu) \propto \rho \propto r^{1/2}(\nu) \propto \nu^{-p/2}$ , where  $\rho$  is the opening angle of dipolar field lines. The longitudinal phase  $\varphi(\nu) = 360^\circ \cdot t(\nu)/P$  is determined by the time of arrival  $t(\nu)$  of a particular detail of emission pattern within the  $360^\circ$  pulse window, where  $P$  is the pulsar period. Usually the reference time of arrival ( $t_0 = 0$ ) corresponds to the fiducial plane containing the pulsar spin axis,  $\Omega$ , the magnetic axis,  $\mathbf{m}$ , as well as the observer,  $\mathbf{O}$  (Fig. 1). The time of arrival of radiation corresponding to a particular feature emitted near the fiducial plane does not depend on frequency (if the dispersive delays are properly removed, Craft 1970). In this paper we will use the term “detail of emission pattern” in several different meanings, such as: the longitude of subpulse peak  $\varphi_s$ , the longitude of the mean profile peak  $\varphi_p$ , the longitude of the profile midpoint  $\varphi_m$ , and mean profile width  $W(\nu) = 2 \cdot \varphi_w(\nu)$  at some intensity level  $w$  referred to the maximum intensity (usually 10% or 50%), where  $\varphi_w(\nu)$  is the longitudinal phase of mean profile corresponding to the  $w$

percent of relative intensity.

Izvekova et al. (1993) were the first to examine the frequency dependence of subpulse versus profile component variations for four pulsars: PSRs B0031–07, B0320+39, B1133+16 and B2016+28, which are well known for the prominent subpulse drift phenomenon (see Table 1). Izvekova et al. (1993) used a technique which did not require simultaneous single pulse observations at different frequencies. They measured the parameter  $P_2$ , which is the spacing between two bands of drifting subpulses, for different frequencies and converted it into a longitude separation,  $\Delta\varphi_s = 360^\circ \cdot P_2/P$ . In the corresponding mean profiles they measured the pulse widths  $\Delta\varphi_{50} = 2\varphi_{50}$  and  $\Delta\varphi_{10} = 2\varphi_{10}$  at 50 and 10 per cent of the maximum intensity, respectively. Izvekova et al. (1993) found that if one presents the frequency dependence of pulsar radiation patterns in the exponential form  $\Delta\varphi_w \propto \nu^{-p_w}$ , then  $p_{50} > p_{10} > p_s$ . In other words, they demonstrated that the longitudes  $\varphi_s$  of subpulse peaks vary with frequency much less than the longitudes of corresponding profile components  $\varphi_{50}$  or  $\varphi_{10}$ . From their sample of four pulsars, typical values obtained are  $p_{50} \sim 0.35$  and  $p_s \sim 0.1$  (Table 1).

As Izvekova et al. (1993) noticed correctly, their results imply that the excitations of subpulse emission do not follow exactly the distribution of excitations leading to the mean emission, which is difficult to reconcile with a simple pulsar picture. However, Gil & Krawczyk (1996) demonstrated that this is exactly what one should expect if the mean pulsar beams have a conal structure. In fact, within a conal model of pulsar beams (Rankin 1993; Gil et al. 1993; Gil & Krawczyk 1996; Mitra & Deshpande 1999) the subpulse enhancement follows a narrow bundle of dipolar field lines, while the mean emission enhancement (corresponding to peaks of the mean profile components) is distributed over a cone (or a number of nested cones) of dipolar field lines (see Fig. 1 for illustration). Thus, the frequency dependence of subpulse and component peak longitudes should, in general,

be different. On the other hand, for a patchy model of the mean pulsar beam (Lyne & Manchester 1988; Manchester 1995), both subpulse enhancements and those related to the profile components follow more or less the same bundles of dipolar field lines. Within such a model, the frequency dependence of subpulse and component peak longitudes should be similar, which is in conflict with available observational data.

In this paper we further discuss the problem of frequency dependence of pulsar radiation patterns, analyzing new single pulse data obtained for PSR B0329+54 simultaneously at 238 and 610 MHz, using the Giant Metrewave Radio Telescope (GMRT). We confirm the conclusion obtained by Gil & Krawczyk (1996) who used averaged data in their analysis, by showing the corresponding effects in single pulse data.

## 2. Single pulse simultaneous dual frequency data of PSR B0329+54

The single pulse simultaneous dual frequency data used in our analysis were taken with the Giant Metrewave Radio Telescope (GMRT) at Khodad in India (see Swarup et al. (1990) for details about the GMRT). The data were obtained by adding the total power detected signals from 12 of the 30 antennas of the GMRT, using the incoherent mode array combiner of the GMRT (see Gupta et al. (2000) for more details about the pulsar mode of operation of the GMRT). The bandwidth used was 16 MHz, divided into 256 spectral channels by the digital back-ends. The raw data were integrated to a time resolution of 0.516 millisecond (corresponding to a pulse longitude resolution of 0.26 degree) before being recorded for off-line analysis, where the data were dedispersed and gated to obtain the single pulse data sequence. A special feature of these observations was that they were carried out at two radio frequencies simultaneously, by splitting the array of 12 antennas in to two sub-arrays – one consisting of 5 antennas operating in the 238 MHz band and the other consisting of 7 antennas operating in the 610 MHz band. After total power detection,

the data from antennas at both frequencies were added together in the incoherent mode array combiner. During the off-line analysis, the pulsar's dispersion curve was used to discriminate between the longitude location of the pulses at the two radio frequencies, thus allowing the recovery of dedispersed pulse trains at the two different radio frequencies from a single raw data set. The technique works as long as the combination of the two chosen frequencies, and the DM and period of the pulsar is such that pulses from the two radio bands (after dispersion) do not overlap. The advantage of the technique is that the data from the two frequencies is completely aligned in time, except for the dispersion delay between the two radio frequencies. This delay is easily and accurately estimated and the two dedispersed data trains are aligned by removing this delay. The data set used here was recorded on 10th August, 1999 and consists of a sequence of 1475 pulses of PSR B0329+54.

The average profiles for PSR B0329+54 obtained at 238 and 610 MHz from this data are shown in Fig. 2. Both profiles show a central core component and the two prominent conal components (one on each side of the core) that are normally easily seen for this pulsar. The radius-to-frequency mapping effect for the average profiles is also clearly seen in this figure, with the conal components at the lower frequency (238 MHz) occurring further away from the central core component than the corresponding conal components at the higher frequency (610 MHz). A sample of selected single pulses at the two frequencies is shown in Fig. 3, along with the integrated profiles for reference. The data for 238 MHz is shown by the thicker lines, whereas the 610 MHz data is shown by the thinner lines. These single pulses are selected on the basis of good signal to noise ratio (at both frequencies) for at least one of the conal components. The threshold used was a peak SNR criteria (in the longitude window for the conal component) of 7 times the rms of the off-pulse noise. This yielded 20 and 16 pulses for the leading and trailing components respectively, from which the 5 best examples – where the sub-pulse shapes at both frequencies are fairly clear and Gaussian-like – were selected for each conal component. The longitude windows used

for the two conal components are shown in the figure by the grey vertical lines in the left hand panels, and are demarcated as “win1” and “win2” for the leading and trailing conal components, respectively.

It is seen that the emission features in the individual pulses also exhibit the radius-to-frequency mapping effect in that the subpulses at the lower frequency appear earlier for the leading conal component and later for the trailing component, when compared with the corresponding feature at 610 MHz. However, the interesting point is that, for all the single pulses shown, the longitudinal separation between the subpulse peaks at the two frequencies is *smaller* than the corresponding separation in the average profile. This is quantified by examining the peaks of the cross-correlation functions (CCFs) for the average profile as well as the individual pulses. These CCFs are displayed in the right hand panel of Fig. 3. The peaks of the CCFs (marked by the open circle symbols) are a measure of the longitudinal separation between the correlating single pulse features at the two frequencies, for the selected conal component. For the average profile, the location of the CCF peaks are marked by the two grey vertical lines in the right hand panel. These correspond to a mean shift of 7 bins (1.82 degrees) of pulse phase (negative) for the leading conal component and 4 bins (1.04 degree) of pulse phase (positive) for the trailing conal component, for the average profile. These two shifts are not equal in amplitude, with the departure from symmetry being about  $(7 - 4)/2 = 1.5$  bins or 0.39 degree. This asymmetry, which is also clearly visible to the eye in Fig. 2, is believed to be due to the effects of retardation and aberration (see Gangadhara & Gupta 2001) which cause the conal beams at different frequencies (emitted at different heights) to be aberrated and retarded by different amounts, leading to increased separation for the leading parts of the profile and reduced separation for the trailing parts of the profile. The retardation-aberration shift of 0.39 degree or 0.77 msec, translates into a difference of emission altitudes of  $\Delta r \sim c 7.7 \times 10^{-4} \text{ s} \sim 2.3 \times 10^7 \text{ cm}$ , where  $c = 3 \times 10^{10} \text{ cm/s}$ . This is perfectly consistent with the empirical radius-to-frequency

mapping given by Kijak & Gil (1998). In fact, for PSR B0329+54 Kijak & Gil (1998) give the emission altitude  $r(\nu) = (5 \pm 0.5) \times 10^7 \nu_{GHz}^{-0.21 \pm 0.07}$  cm. For our frequencies of 0.24 and 0.61 GHz, the emission altitudes are about  $7 \times 10^7$  cm and  $5 \times 10^7$  cm, respectively. Thus, the difference in altitudes is  $\Delta r \sim 2 \times 10^7$  cm, in good agreement with  $\Delta r \sim 2.3 \times 10^7$  cm inferred from the observed retardation-abberation shift. These numbers are also in good agreement with the estimates for emission heights for the conal components for this pulsar obtained by Gangadhara & Gupta (2001) using accurate measurements of the retardation and aberration effects.

The typical deviation of the peak of the CCF for the individual pulses with respect to that for the average profile for the corresponding conal component, is 2 to 3 bins (0.52 to 0.78 degree) of longitude, with a minimum to maximum range of 0 to 5 bins (0 to 1.3 degree). There appears to be some evidence that these shifts in the CCF peaks are systematically larger for the trailing conal component. Note that there are practically no cases where the magnitude of the shift for the individual subpulse is more than that for the corresponding conal component in the average profile.

The above conclusions are further quantified by studying the distribution of the CCF peaks for the individual pulse cases, compared to the peak of the CCF for the average profile for the corresponding conal component. This is illustrated in Fig. 4 which shows the histograms of the distributions of the CCF peaks obtained for the selected single pulses for a SNR threshold of 5 times the off-pulse rms noise. The results for the two conal components are shown as separate histograms, for the respective windows. The total number of pulses that meet the threshold criteria are 56 and 57 for the two conal components, out of a total of 1475 pulses. The actual quantity used for the histogram plots is the difference between the CCF peak for the individual pulse and the CCF peak for the average profile for the corresponding conal component. Thus the zero position bin in the histogram corresponds

to cases of single pulses where the shift in the subpulse at the two frequencies is the same as the corresponding shift in the average profile. These plots clearly show that the CCF peaks for the individual pulses are asymmetrically distributed with respect to the CCF peak for the average profile for the corresponding conal component. They also show that the magnitude of the shift is somewhat larger for the trailing component, as compared to the leading component, with mean values for the shifts being -2.5 bins (-0.65 deg) and 1.4 bins (0.36 degree), respectively.

These results are consistent with those of Izvekova et al. (1993). All these are summarized in Table 1. Although there are differences from pulsar to pulsar, the results in Table 1 reinforce the conclusion that the frequency dependence of subpulse patterns is apparently weaker than the frequency dependence of corresponding features in the average profile. The exponents quoted for PSR B0329+54 (0.14 and 0.07 for mean profile and single pulses, respectively) refer to average values following from estimates obtained for the left (L) and right (R) side of the pulse profiles, after corrections for retardation-aberation shift of about 1.5 bin (0.4 degree of longitude). In the next section we argue that this different frequency dependence of subpulses and corresponding profile components is natural, provided that the mean pulsar beam has a conal structure and the subpulse emission is associated with narrow bundles of dipolar magnetic field lines. We assume that only one bundle (controlling the subpulse-associated plasma flow) is related with one subpulse observed simultaneously at the two frequencies.

### 3. Structure of pulsar beams

It is widely believed that pulsar elementary emission is relativistically beamed tangentially to dipolar magnetic field lines. Thus, the geometry of the emission region can be described by the opening angle  $\rho(\nu) = 1^\circ.25 \cdot s \cdot r_6(\nu)^{1/2} P^{-1/2}$  (Fig. 1), where  $P$  is the pulsar period,

and  $r_6 = r(\nu)/R$  is the frequency dependent emission altitude in units of stellar radius  $R = 10^6$  cm. The mapping parameter ( $0 \leq s \leq 1$ ) is determined by the locus of dipolar field lines on the polar cap ( $s = 0$  at the pole and  $s = 1$  at the polar cap edge). Thus,  $s = d/r_p$ , where  $d$  is the distance from the magnetic axis,  $\mathbf{m}$ , to a field line on the polar cap corresponding to a certain detail of the emission pattern, and  $r_p = 1.4 \cdot 10^4 P^{-1/2}$  cm is the canonical polar cap radius. According to the widely accepted concept of radius-to-frequency mapping, the higher frequencies are emitted at lower altitudes than the lower frequencies. Kijak & Gil (1998) have found an empirical formula describing an altitude of the emission region corresponding to a frequency  $\nu_{\text{GHz}}$  (in GHz) as

$$r_6 \approx 50 \cdot \nu_{\text{GHz}}^{-0.21} \cdot \tau_6^{-0.07} \cdot P^{0.33} \quad (1)$$

where  $\tau_6$  is the pulsar characteristic age in million years and  $P$  is the pulsar period. This empirical relationship will be used in our model calculations.

To perform geometrical calculations of the radiation pattern one has to adopt a model of instantaneous energy distribution on the polar cap. We will assume that at any instant the polar cap is populated by a number of features with a characteristic dimension  $\mathcal{D}$  (e.g. Gil & Sendyk 2000), each delivering to the magnetosphere a column of plasma flowing along separate bundle of dipolar magnetic field lines. These plasma columns are supposed to be sources of the narrow-band radiation, with different radio frequencies emitted at different altitudes, as described by the radius-to-frequency mapping law (Kijak & Gil 1998). Thus, one plasma column illuminates different spots at different frequencies. Some of these spots can be intersected by the line of sight (LOS henceforth) and thus observed simultaneously at two frequencies. Each feature is modelled at the polar cap by a gaussian intensity distribution

$$I_i = \exp(-\kappa l^2/\mathcal{D}^2) \quad (2)$$

where  $l^2 = d^2(\varphi) + d_i^2 - 2d(\varphi)d_i \cdot \cos[\sigma(\varphi) - \sigma_i]$ . Here the pairs  $[d_i, \sigma_i]$  and  $[d(\varphi), \sigma(\varphi)]$  are

polar coordinates of the  $i$ -th feature (maximum intensity) and the observer's position on the line of sight (projected onto the polar cap), respectively. The instantaneous emission of the  $n$ -th pulse is described by  $I_n(\varphi) = \sum_{i=1}^{K_n} I_i(\varphi)$ , where  $K_n$  is the number of adjacent features contributing to the radiation observed in the  $n$ -th pulse at a longitude  $\varphi$ . The average pulse profile is therefore  $I(\varphi) = \frac{1}{N} \sum_{n=1}^N I_n(\varphi)$ , where  $N$  is the number of averaged single pulses.

The azimuthal angle variations of the  $i$ -th feature are described by

$$\sigma_i = \arctan[\sin \varphi_i \cdot \sin(\alpha + \beta) \cdot \sin \alpha / \cos(\alpha + \beta) - \cos \alpha \cdot \cos \rho_i] - n \cdot \Delta\sigma \quad , \quad (3)$$

where

$$\rho = 2 \cdot \arcsin[\sin^2(\varphi/2) \cdot \sin \alpha \cdot \sin(\alpha + \beta) + \sin^2(\beta/2)]^{1/2} = 1.^{\circ}25 \cdot r_6(\nu)^{1/2} P^{-1/2} \quad , \quad (4)$$

and  $\Delta\sigma$  is the change of azimuthal angle per one pulsar period,  $\alpha$  is the inclination angle between the rotation and magnetic axes and  $\beta$  is the impact angle – the angle of the closest approach of the line of sight to the magnetic axis (Figs. 1, 5 and 6).

Any specific intensity distribution can be transferred along dipolar field lines to the emission region and then along straight lines to a given observer specified by inclination and impact angles ( $\alpha, \beta$ ). Thus, knowing a distribution of opening angles  $\rho_i(\nu) = 1.^{\circ}25(d_i/r_p)r_6^{1/2}(\nu)P^{-1/2}$  corresponding to instantaneous radiation, one can calculate the longitude of an  $i$ -th detail of the emission pattern  $\varphi_i = 2 \arcsin \left\{ \left[ \sin \left( \frac{\rho_i - \beta}{2} \right) \cdot \sin \left( \frac{\rho_i + \beta}{2} \right) \right] / [\sin \alpha \cdot \sin(\alpha + \beta)] \right\}^{1/2}$  at a given frequency  $\nu$  (Gil 1981). The mean profile can be obtained by a simple averaging of individual waveforms, which can in principle vary in time, depending on the adopted model of distribution of instantaneous arrangement of energy on the polar cap.

Gil & Krawczyk (1996) and Gil & Sendyk (2000) argued that the nested cone structure of mean pulsar beams is induced by the vacuum gap  $\mathbf{E} \times \mathbf{B}$  drift (Ruderman & Sutherland 1975), which forces the subpulse-associated plasma columns to rotate around the magnetic

axis. This model suggests a simple and natural relationship between a sequence of single pulses and features of mean emission. It is also very convenient for geometrical simulations, because the azimuthal angle  $\sigma$  (eq. 3) of each plasma column varies regularly with time (sequential pulse number). The frequency dependence of pulsar emission patterns within such a model is qualitatively illustrated in Fig. 1. The subpulse-associated plasma columns corresponding to the half power beam width of the subpulse emission (thin small circles marked by  $S(\nu)$ ), which will be called spots, perform a circumferential motion around the magnetic axis  $\mathbf{m}$ , in which the azimuthal angle  $\sigma$  varies with time while the opening angle  $\rho(\nu)$  remains constant. This motion determines the cones (thick large circles) of the maximum average intensity with the opening angles  $\rho_1$  and  $\rho_2$  at frequencies  $\nu_1$  and  $\nu_2$ , respectively. The frequency dependent longitude  $\varphi_p(\nu)$  of the profile component is determined by the intersection of the line of sight with the average cone at the frequency dependent opening angle  $\rho(\nu)$ . The frequency dependent longitude  $\varphi_s(\nu)$  of subpulse peak is determined by the local maximum intensity along the cut of the line of sight through the subpulse spot. These cuts are marked by dashed lines (shorter dash for  $S'(\nu_1)$  and longer dash for  $S(\nu_2)$ , respectively). The position of the spot  $S$  was chosen in such a way that  $\varphi_s(\nu_1) = \varphi_p(\nu_1)$ . This is however a special case, which does not hold for the spot  $S'$ , in which case the longitude of the subpulse peak  $\varphi'_s(\nu_1)$  is different from the longitude of a corresponding component  $\varphi'_p(\nu_1)$ . When the frequency changes from  $\nu_1$  to  $\nu_2$ , the subpulse peak longitude changes from  $\varphi_s(\nu_1)$  to  $\varphi_s(\nu_2)$ , while the corresponding profile peak longitude changes from  $\varphi_p(\nu_1)$  to  $\varphi_p(\nu_2)$ . Note that  $\Delta\varphi_p = \varphi_p(\nu_2) - \varphi_p(\nu_1)$  is generally larger than  $\Delta\varphi_s = \varphi_s(\nu_2) - \varphi_s(\nu_1)$ . This is consistent with observations of four pulsars published by Izvekova et al. (1993) and confirmed in this paper for yet another pulsar PSR B0329+54 (Table 1).

It is important to note that in this model,  $\Delta\varphi_s \leq \Delta\varphi_p$ , is *always* true. The equality condition holds only for two special cases: (i)  $\sigma \approx 90^\circ$  and  $\beta \approx 0^\circ$  and (ii)  $\sigma \approx 0^\circ$ . The

latter case is trivial since it corresponds to  $\Delta\varphi_s = \Delta\varphi_p \approx 0^\circ$  for which both subpulses are observed at the fiducial phase; while the former one corresponds to central cut of the LOS across the beam. For all cases other than these two,  $\Delta\varphi_s < \Delta\varphi_p$  is strictly true. This prediction of the model has been shown to be true in the observed data (Figs. 2 and 3) and will be shown to hold for the simulated synthetic data as well. It should be emphasized that we consider only cases in which both higher and lower frequency spots illuminated by the same single subpulse-associated plasma column are observed (i.e. intersected by the LOS). The cases in which subpulse at one of the two frequencies is missing are not interesting for the present analysis, as no frequency dependent effect can be measured for these.

After qualitative illustration of the problem (Fig. 1) we now explore it quantitatively by means of geometrical simulations. Although we did not intend to model exactly the pulse profiles of PSR B0329+54, we adopted in our calculation the values of  $P = 0.7$  s and  $\dot{P} = 2 \cdot 10^{-15}$ . Thus, our model of the polar cap or the corresponding instantaneous radiation beam presented in Fig. 5 corresponds in a sense to PSR B0329+54. We followed Gil & Sendyk (2000) (their eqs. [11] and [12]) for description of the polar cap arrangement. The characteristics of instantaneous radiation are imprinted on the polar cap, transmitted along dipolar field lines to the radio emission altitudes and then emitted to a particular observer along straight paths. The circumferential motion of sparks around the magnetic axis (Fig. 5) will lead to a nested cone structure of the average radiation beam, as presented in Fig. 6. The adopted inclination angle  $\alpha = 30^\circ$  and four line of sight trajectories correspond to impact angles  $\beta = 0, 3.3, 5.0$  and  $6.6$  degrees, respectively. We performed calculations for the two frequencies 238 and 610 MHz. Hence, each line of sight trajectory bifurcates when projected onto the surface of the polar cap.

The results of calculations of radiation waveforms corresponding to emission patterns presented in Figs. 5 and 6 are shown in Fig. 7. Four vertical panels correspond to different

impact angles  $\beta = 0, 3.3, 5.0$  and  $6.6$  degrees, respectively. The broader emission at  $238$  MHz is shown by dashed lines and higher frequency radiation at  $610$  MHz is shown by solid lines. Both instantaneous single pulse and mean profile are presented for each impact angle. We have calculated a long sequence of single pulses to make sure the mean profile is stable. We selected pulse #4 in our sequence (for no particular reason) and show its profile for each impact angle at the two frequencies.

The first panel corresponds to a central cut of the line of sight with the impact angle  $= 0^\circ$  and, of course,  $\sigma \sim 90^\circ$ . In this case the longitudinal difference of subpulse and profile component peaks occurring at different frequencies is exactly the same ( $\Delta\varphi_s^{max} = \Delta\varphi_p$ ). This can be seen from both visual inspection of the pulse profiles and from the CCF analysis. The CCF computed separately for left (L) and right (R) component, peaks at the same lag in both mean and single pulses. However, as  $\beta$  increases, the difference for subpulses becomes smaller and smaller as compared with a corresponding difference for peaks of profile components. This translates into CCF lags which are smaller for single pulses than for mean pulses. The lag difference is about  $0.5, 1.0$  and  $2.0$  degrees for  $\beta$  values of  $3.3, 5.0$  and  $6.6$  degrees, respectively. This can be compared with Fig. 3, where the mean lag difference is about  $2$  sample bins or  $0.5$  degrees of longitude. Thus, the actual data presented in Fig. 3 correspond to a modelling case with  $\beta \sim 3$  degrees (see Fig. 7).

Another interesting, though obvious property is that the frequency separation disappears near the fiducial longitude  $\varphi = 0^\circ$ , as in the actual data presented in Figs. 2 and 3. We have selected three central subpulses marked by 1, 2 and 3 in Fig. 7. The CCF computed for these subpulses show lags near zero in Fig. 8 (for the subpulse 1 the lag is exactly zero). The explanation of this effect is simple and natural. The fiducial longitude was chosen in such a way that it corresponds to the fiducial plane containing both the  $\Omega$  and  $\mathbf{m}$  axes as well as the observer  $\mathbf{O}$ . The divergence of dipolar magnetic field lines does not

affect longitudinal phases of the observed radiation emitted exactly at this plane (subpulse 1) and affects it only slightly near this plane (subpulses 2 and 3).

In our simulations we have not included the effects of retardation and aberation, which were unequivocally detected in our high resolution, simultaneous dual frequency single pulse data. These effects shift the entire low frequency emission patterns towards earlier phases (leading side) with respect to high frequency patterns. This results in larger frequency difference on the left (L) than on the right (R) side of the profile, thus producing the asymmetrical CCF lags seen in Fig. 3. However, the deviation of single pulse lags from mean pulse lags does not depend on the retardation-aberation shift (see Fig. 2), so our symmetrical model CCF can be compared with the asymmetrical CCF computed for the actual data.

#### 4. Discussion and conclusions

The observed emission patterns of pulsar radio emission are usually frequency dependent. The longitudes of details of pulse profiles appear earlier/later for the leading/trailing side of the pulse window, as frequency decreases. This is well understood in terms of the radius-to-frequency mapping and diverging nature of dipolar magnetic field lines in the radio emission region. However, in PSR B0329+54 and four other pulsars (Table 1) it has been observed that for emission at two different frequencies, the difference in longitudes of subpulse peaks is generally smaller than the difference in longitudes of corresponding component peaks. This suggests that the subpulse and profile component excitations do not follow the same bundles of dipolar field lines, which appears surprising at first sight. However, we argued in this paper that this is exactly what one should expect if:

- (i) the subpulse enhancements are related to relativistic plasma columns following a

narrow (and separated from each other) bundle of dipolar field lines, with different frequencies generated at different altitudes  $r_6(\nu) = r(\nu)/R$ ,

- (ii) the profile component enhancements are related to the conal structure of the mean pulsar beam, and
- (iii) the line of sight trajectory of the observer across the beam is neither central nor grazing (i.e. the impact angles  $0 < \beta < \rho_b$ , where  $\rho_b = 1^\circ.25 r_6^{1/2} P^{-1/2}$  is the opening angle of the full pulsar beam). Particularly, for PSR B0329+54 we deduced the impact angle  $\beta \approx 3^\circ$ , which agrees well with other independent estimates from about  $2^\circ$  (Rankin 1993) to about  $4^\circ$  (Gil and Lyne 1995).

In deriving our conclusions, we have made a number of well justified assumptions, which we summarize below:

- (1) The pulsar radiation is relativistically beamed along dipolar lines of a global magnetic field of the neutron star. This is a generally well accepted assumption.
- (2) The narrow-band pulsar radio emission follows the radius-to-frequency mapping  $r = r(\nu)$ . In our calculations we used a specific form of the empirical relation obtained by Kijak & Gil (1998). Although, the actual form of the radius-to-frequency mapping is not important for our general conclusions (as long as the higher frequencies are generated closer to the polar cap than the lower ones), this relation is strongly supported by the retardation-aberation shift clearly revealed in our high-resolution, simultaneous dual frequency data.
- (3) The instantaneous emission beam consist of a number of subpulse-associated beams emitted by the spark-associated plasma columns. Thus, we invoke a non-stationary model of inner accelerator discharge via a number of isolated sparks (Sturrock 1971; Ruderman & Sutherland 1975; Gil & Mitra 2001).

(4) The structure of mean pulsar beam results from a behaviour of subpulse-associated beams averaged over time intervals much longer than the pulsar period. In our model these beams perform a circumferential motion around the magnetic axis following the  $\mathbf{E} \times \mathbf{B}$  drift motion of sparks on the polar cap. Strong observational evidence of such circumferential motions has been recently presented by Deshpande & Rankin (1999, 2001).

The model of the polar cap arrangement we have adopted here is highly symmetric, which simplifies geometrical calculations. However, our general conclusions do not depend on any specific details of this model, as long as the instantaneous beam is organized into a group of isolated subbeams (Fig. 5) and the average beam has a conal structure (Fig. 6). In our model this conal structure is caused by the circumferential motion of spark-associated, subpulse-producing plasma columns around the axis of symmetry (magnetic axis). For a convenience, we have calculated the emission patterns using a specific velocity of circumferential motion following from the  $\mathbf{E} \times \mathbf{B}$  drift applied to sparks (eq. [14] in Gil & Sendyk 2000), although the value of this velocity is not critical for our results. Our general conclusions apply to a more general picture of the organization of pulsar beams, in which enhancement of excitations leading to subpulses and corresponding profile component, respectively, do not follow each other. We consider the  $\mathbf{E} \times \mathbf{B}$  drift induced model as the simplest and most natural, but the reason for the formation of the conal structure of the mean pulsar beam is not important for our conclusions. We would also like to emphasize that our conclusions do depend sensitively on the impact angles  $\beta$  of the closest approach of the line of sight to the magnetic axis  $\mathbf{m}$  (Fig. 1) but they are rather independent of the inclination angles  $\alpha$ .

To conclude, we have demonstrated in this paper that the angular beaming model of instantaneous emission accompanied by the conal model of mean emission predict

frequency dependent properties of pulsar radiation that match well with those observed in the simultaneous, dual frequency single pulse data of PSR B0329+54 that is reported here. This model also explains the earlier observations reported for four other pulsars – PSRs B0031–07, B0320+39, B1133+16 and B2016+28. We therefore conclude that, at least in these pulsars, the mean pulsar beams have a conal structure, possibly induced by the circumferential  $\mathbf{E} \times \mathbf{B}$  drift motion of subpulse-associated beams. Thus, our paper provides independent support for the nested-cone model of pulsar beams (Rankin 1993; Gil et al. 1993; Kramer et al. 1994; Mitra & Deshpande 1999; Gangadhara & Gupta 2001).

This paper is supported in part by the Grant 2 P03D 008 19 of the Polish State Committee for Scientific Research. We thank an anonymous referee for useful comments. We are thankful to Drs. D. Mitra and B. Zhang for helpful discussions. We thank E. Gil, O. Maron and M. Sendyk for technical assistance. We also thank the staff of the GMRT that made these observations possible and specifically Dr. B.C. Joshi for this particular data set. GMRT is run by the National Centre for Radio Astrophysics of the Tata Institute of Fundamental Research.

## REFERENCES

Asseo, E., Melikidze, G. 1998, MNRAS, 301, 59

Cordes, J.M. 1992, in IAY Coll. 128, ed. T.H. Hankins, J.M. Rankin & J.A. Gil (Zielona Gora: Pedagogical Univ. Press), 253

Cordes, J.M. 1978, ApJ, 222, 1006

Craft, H.D. 1970, Rept. No. 399, Cornell University

Deshpande, A.A., & Rankin, J.M. 1999, ApJ, 524, 1008

Deshpande, A.A., & Rankin, J.M. 2001, MNRAS, 322, 438

Gangadhara, R.T.G., & Gupta Y. 2001, ApJ, 555, 31

Gil, J. 1981, Acta Phys. Pol., B12, 1081

Gil, J., Kijak, J., Seiradakis, J.H. 1993, A&A, 272, 268

Gil, J., Lyne, A.G. 1995, MNRAS, 276, L55

Gil, J., & Krawczyk, A. 1996, MNRAS, 280, 143

Gil, J., Sendyk, M. 2000, ApJ, 541, 351

Gil, J., & Mitra, D. 2001, ApJ, 550, 383

Gupta, Y., Gothoskar, P. G., Joshi, B. C., Vivekanand, M., Swain, R., Sirothia, S., & Bhat, N.D.R. 2000, in IAU Colloquium 177: Pulsar Astronomy – 2000 and Beyond, eds. M. Kramer, N. Wex & R. Wielebinski, ASP Conf. Series, 105, 277

Izvekova, V.A., Kuzmin, A.D., Lyne, A.G., Shitov, Yu.P., & Smith, F.G. 1993, MNRAS, 261, 865

Kazbegi, A., Machabeli, G., Melikidze, G., Shukre, C. 1996, A&A, 309, 515

Kijak, J., Gil, J. 1998, MNRAS, 299, 855

Kramer, M., Wielebinski, R., Jessner, A., Gil, J.A., Seiradakis, J.H. 1994, A&ASuppl. Ser., 107, 515

Lyne, A.G., Manchester, R.N. 1998, MNRAS, 234, 477

Manchester, R.N. 1995, JA&A, 23, 283

Melikidze, G.I., Gil, J., & Pataraya, A.D. 2000, ApJ, 544, 1081

Mitra, D., & Deshpande, A.A. 1999, A&A, 346, 906

Rankin, J.M. 1983, ApJ, 274, 333

Rankin, J.M. 1990, ApJ, 352, 247

Rankin, J.M. 1993, ApJ, 405, 285

Ruderman, M.A., Sutherland, P.G. 1975, ApJ, 196, 51

Sturrock, P.A. 1971, ApJ, 164, 529

Swarup, G., Ananthakrishnan, S., Subrahmanya, C. R., Rao, A. P., Kulkarni, V. K., & Kapahi, V. K. 1990, in High Sensitivity Radio Astronomy, ed. N. Jackson & R.J. Davis (Cambridge Univ. Press)

Usov, V.V. 1987, ApJ, 320, 333

Table 1. Frequency dependence of pulse profile characteristics  $\varphi_i \propto \nu^{-p_i}$ .

PSR B	$\varphi_{50} \propto \nu^{-p_{50}}$	$\varphi_{10} \propto \nu^{-p_{10}}$	$\varphi_c \propto \nu^{-p_c}$	$\varphi_s \propto \nu^{-p_s}$	Ref.
0329+54			0.14	0.07	(2)
0031-07	0.45	0.35		0.05	(1)
0320+39	0.34	0.18		0.15	(1)
1133+16			0.25	0.06	(1)
2016+28	0.35	0.2		0.17	(1)

Note. —  $\varphi_{50}$  - half width  $W_{50} = 2 \cdot \varphi_{50}$  of the profile at 50% maximum intensity,  $\varphi_{10}$  - half width  $W_{10} = 2 \cdot \varphi_{10}$  of the profile at 10% maximum intensity,  $\varphi_c$  - longitude of profile component peak,  $\varphi_s$  - longitude of subpulse peak, Ref: (1) Izvekova et al. (1993), (2) this paper

## Figure captions

Fig. 1.— The conal model for the mean pulsar beam. The geometry of observation is determined by the inclination angle  $\alpha$  between the magnetic axis  $\mathbf{m}$  and the spin axis  $\mathbf{\Omega}$  and the impact angle  $\beta$  of the closest approach of the line of sight (observer  $\mathbf{O}$ ) to the magnetic axis  $\mathbf{m}$ . The plane containing the spin axis  $\mathbf{\Omega}$ , the magnetic axis  $\mathbf{m}$  and the observer  $\mathbf{O}$  defines the fiducial longitude  $\varphi = 0^\circ$ . The frequency dependent position of any observed feature in the beam pattern is described by two angles: the frequency dependent opening angle  $\rho(\nu)$  between the  $\mathbf{m}$  axis and the line of sight and by the azimuthal angle  $\sigma$  between the fiducial plane and the plane of dipolar field lines associated with a particular feature. The subpulse emission is associated with the frequency dependent subpulse spots  $S(\nu)$  and the profile components are associated with the frequency dependent cones. The longitudes of subpulse peaks  $\varphi_s(\nu)$  and profile peaks  $\varphi_p(\nu)$  are marked, with  $\nu_2 > \nu_1$ .

Fig. 2.— Average profiles at 238 and 610 MHz for PSR B0329+54, obtained from the simultaneous dual frequency observations. The darker curve is for 238 MHz and the lighter one for 610 MHz. Each sample bin corresponds to 0.26 degrees of longitude.

Fig. 3.— The observed frequency dependence of radio emission patterns in PSR B0329+54. Selection of 10 single pulses from the observations is shown (at both frequencies) in the left hand panels. The darker curves are for 238 MHz and the lighter curves for 610 MHz. The average profile (top panel) is shown truncated in amplitude to highlight the conal components. The right hand panels show the cross-correlation functions for the relevant conal component, with the peaks marked by the open circle symbols. Each bin or lag corresponds to 0.26 degrees of longitude.

Fig. 4.— Histograms of the distributions of the location of the CCF peaks obtained for the leading conal component (top panel) and trailing conal component (bottom panel) for the

selected single pulses. The locations are taken with respect to the location of the peak of the CCF for the average profile for the corresponding conal component.

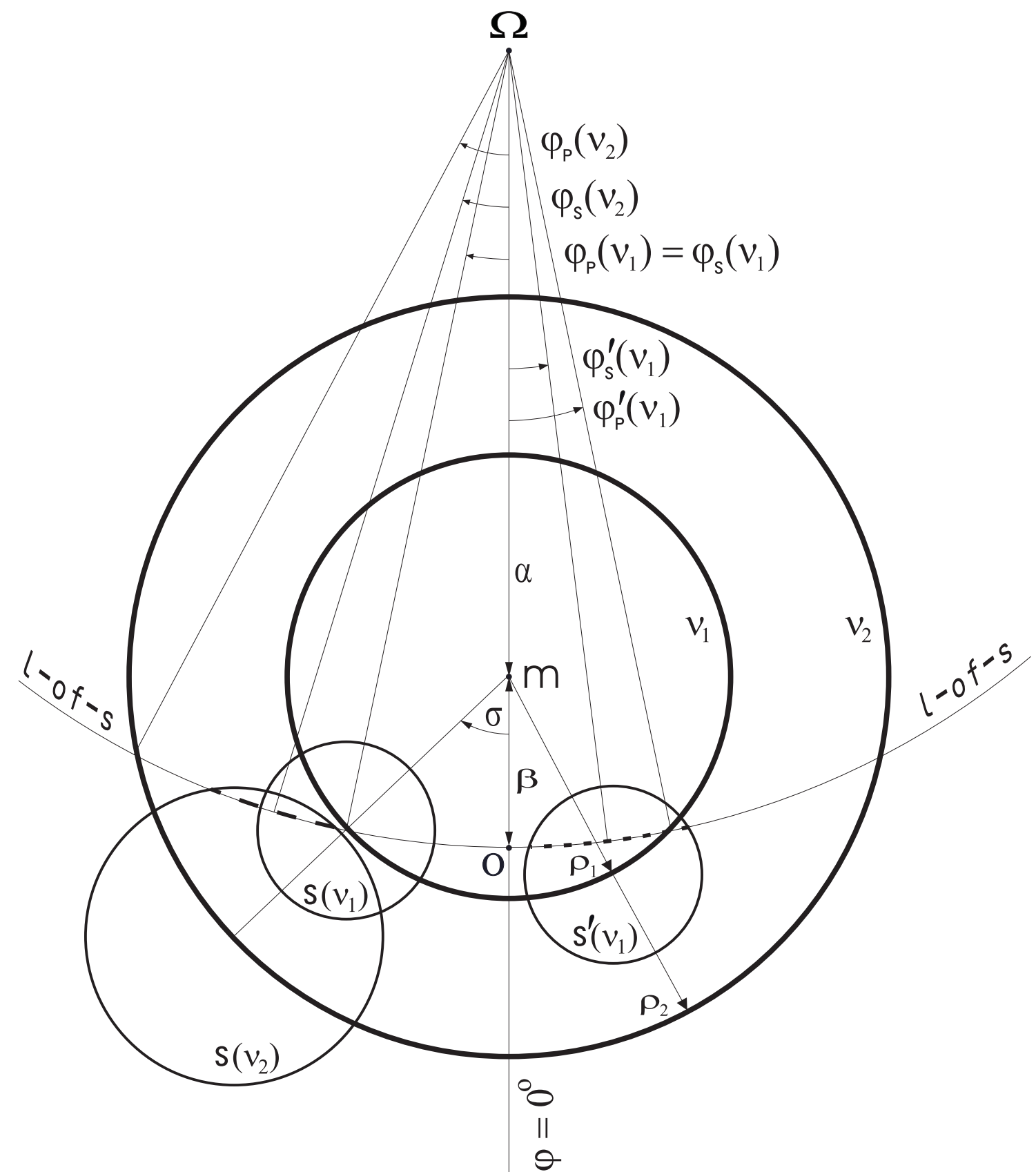
Fig. 5.— Instantaneous arrangement of sparks on the Polar Cap (or instantaneous pulsar beam projected onto the PC along dipolar field lines) corresponding to the simulated pulse #4 presented in Fig. 7. Four different (frequency bifurcated) line of sight trajectories with impact angles  $\beta = 0.0, 3.3, 5.0, 6.6$  degrees corresponding to frequencies 238 and 630 MHz are presented. The pulsar rotates clock-wise, so the leading part of the pulse corresponds to the right side of this figure (or left if viewed from the spin axis  $\Omega$ ). The inclination angle between the magnetic axis (marked by the central dot) and the spin axis is 30 degrees.

Fig. 6.— The average structure of the polar cap (or mean pulsar beam projected onto the PC) resulting from the circumferential motion of sparks (or subpulse beams) around the magnetic axis (marked by the central dot). For explanation of different line of sight trajectories see caption for Fig. 5.

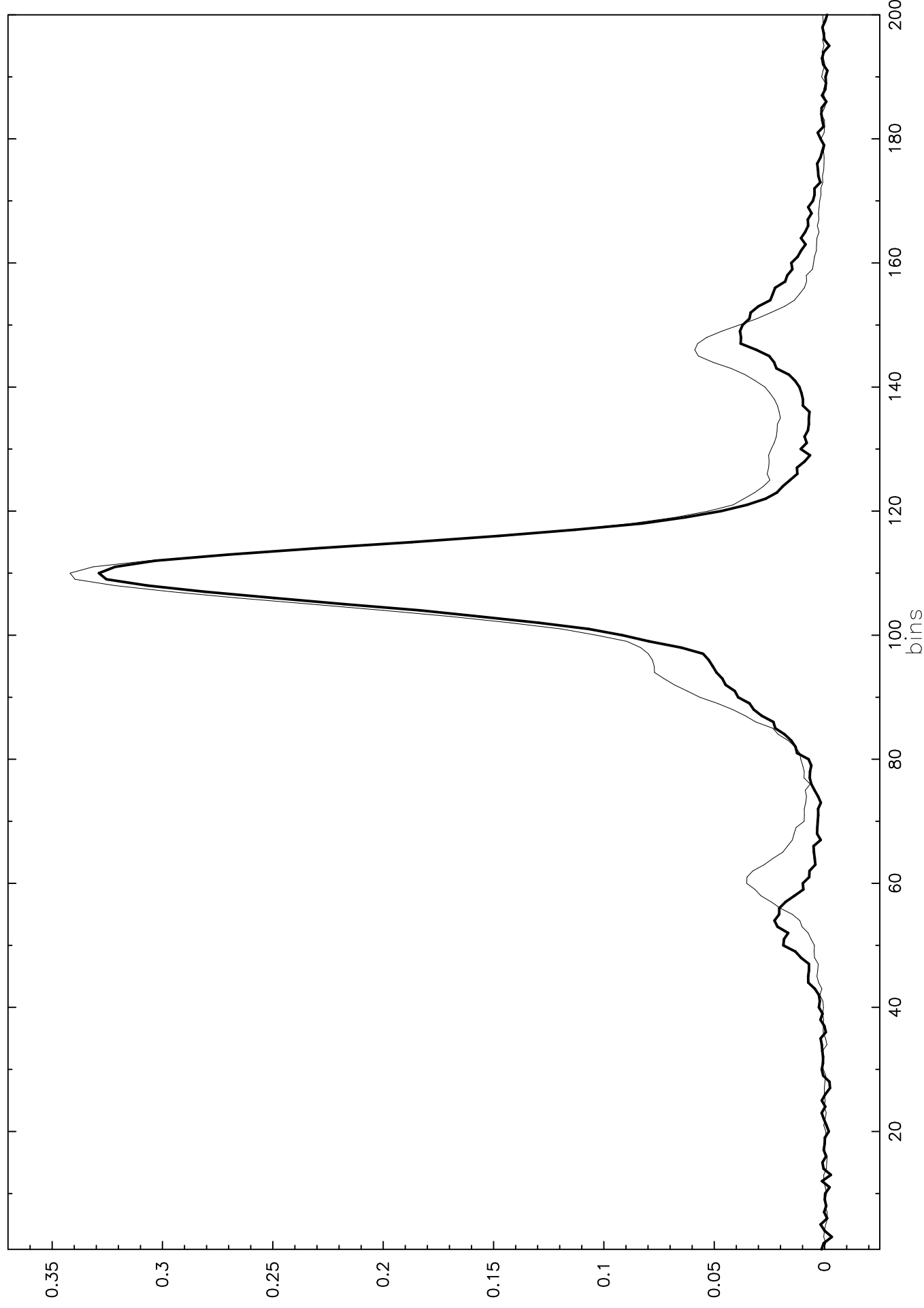
Fig. 7.— The frequency dependence of pulsar radiation patterns corresponding to Figs. 5 and 6. In the analogy to Fig. 3, the left panels present the pulses, while the right panels present the corresponding cross-correlation functions (CCF). Each vertical panel presents the integrated profile and a single pulse for a given impact angle  $\beta = 0.0, 3.3, 5.0$  and 6.6 degrees. The symbols L and R correspond to the leading and trailing conal components of the profile, respectively. One can easily notice from both visual inspection and from the CCF analysis that the difference in longitudes of pulse features occurring at 238 and 610 MHz depends on the impact angle  $\beta$  (closest approach of the observer to the beam axis). For  $\beta = 0$ , this separation is the same for both single pulses and integrated profiles. However, at larger impact angles the separation for subpulses is smaller than for a corresponding profile components. It is worth noting that longitudes of subpulse peaks and corresponding profile components are the same near the fiducial phase  $\varphi = 0^\circ$  like in the real data presented in

Figs. 2 and 3 (see CCF analysis in Fig. 8 corresponding to central subpulses marked by 1, 2 and 3 in this figure).

Fig. 8.— The cross-correlation function (CCF) calculated for three subpulses marked by 1, 2 and 3 in Fig. 7. The maximum of each function is at zero lag, meaning that subpulses near the fiducial longitude  $0^\circ$  (profile centre) appear in the same phases at both frequencies, unlike the side subpulses analysed in Fig. 7.

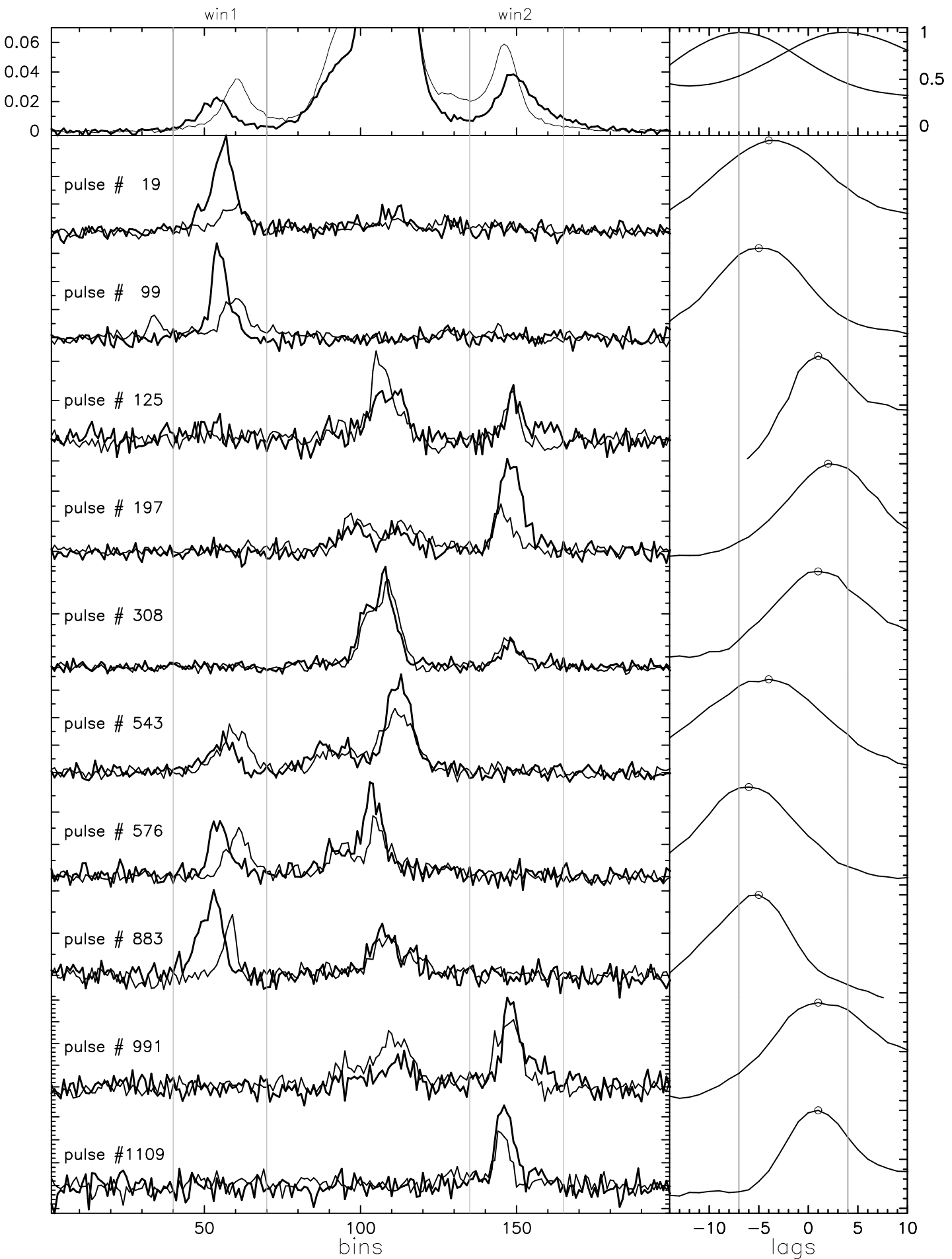


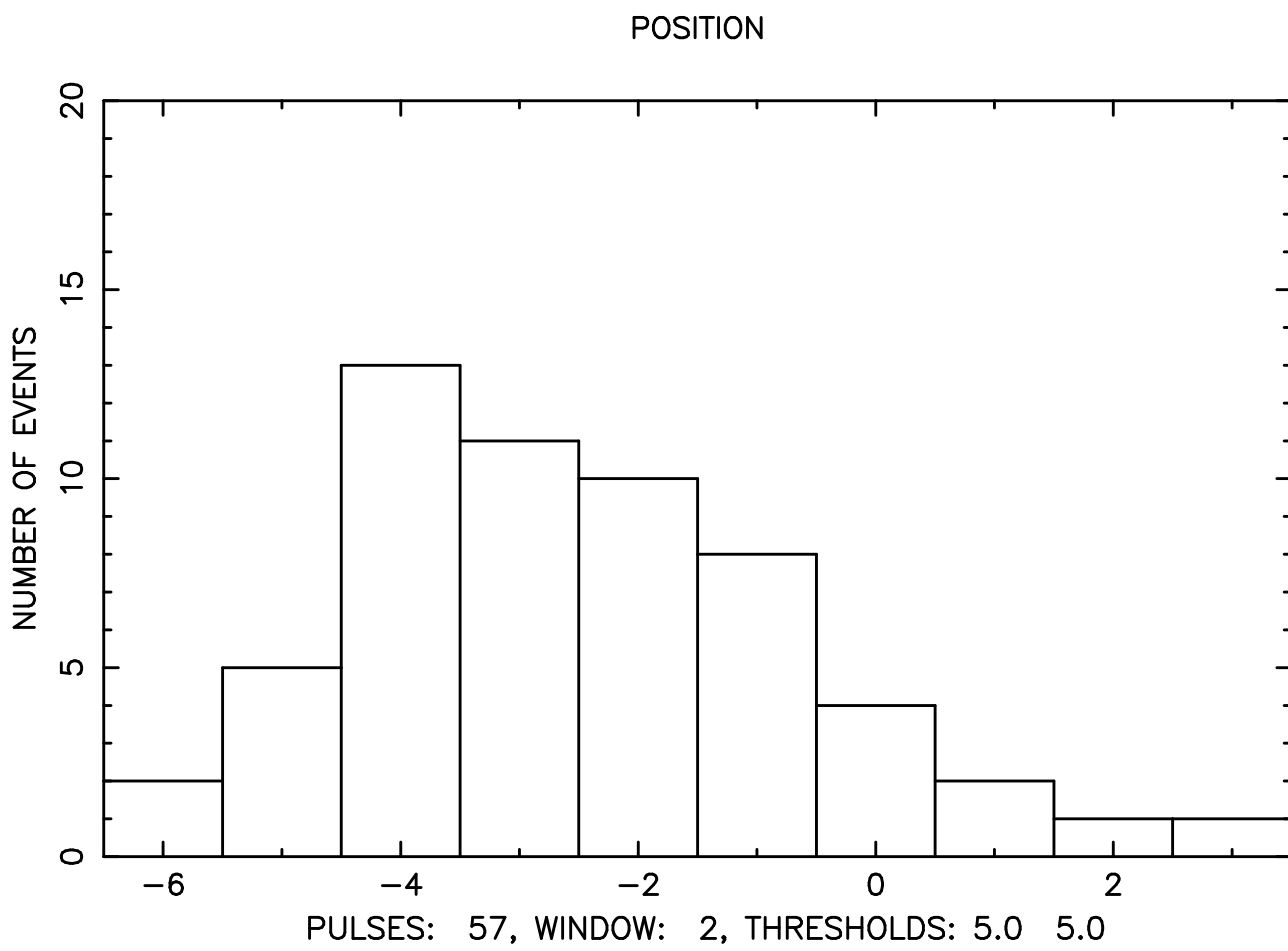
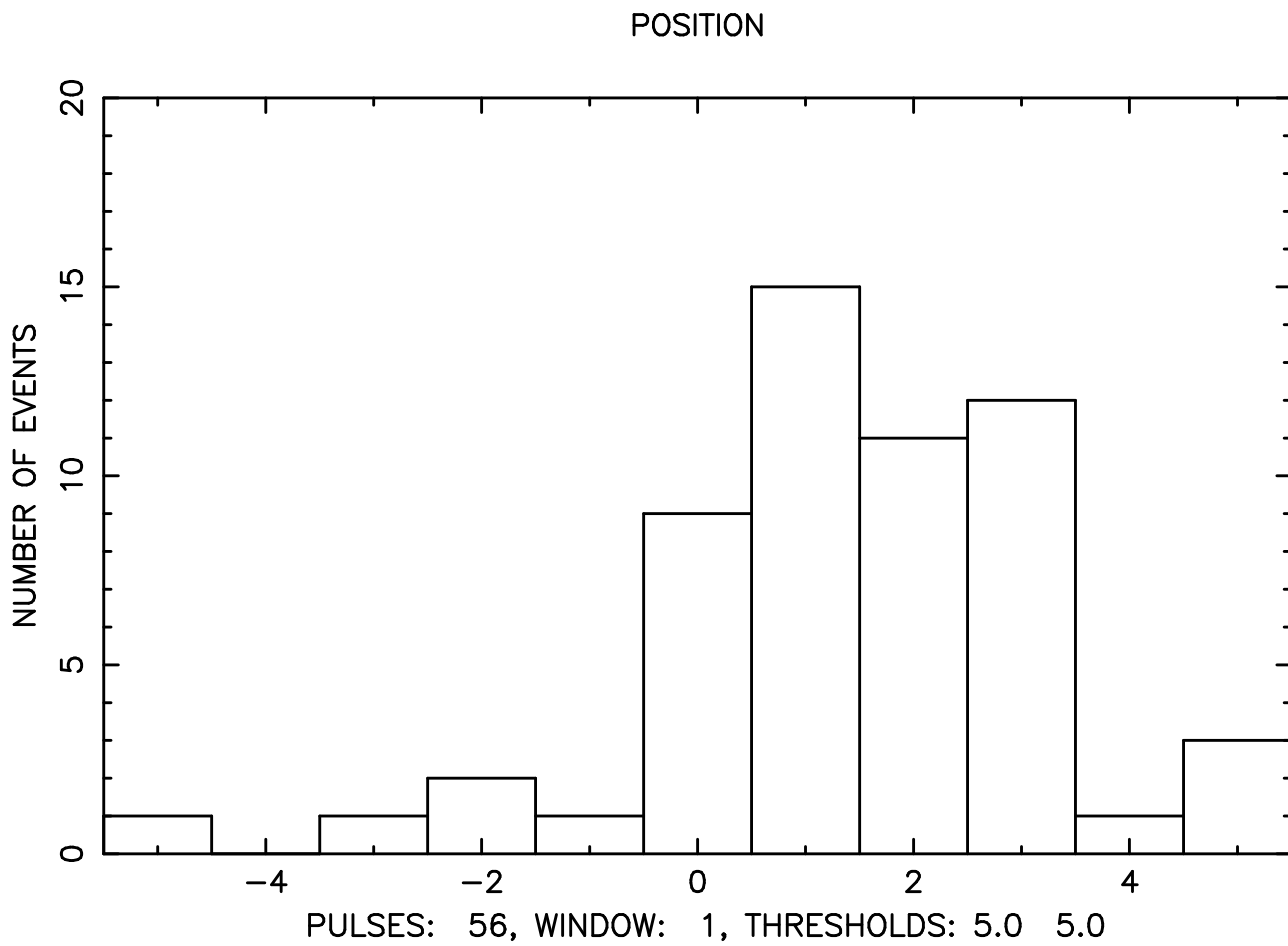
PSR B0329+54 at 610 and 238 MHz



PSR B0329+54 at 610 and 238 MHz

CCF

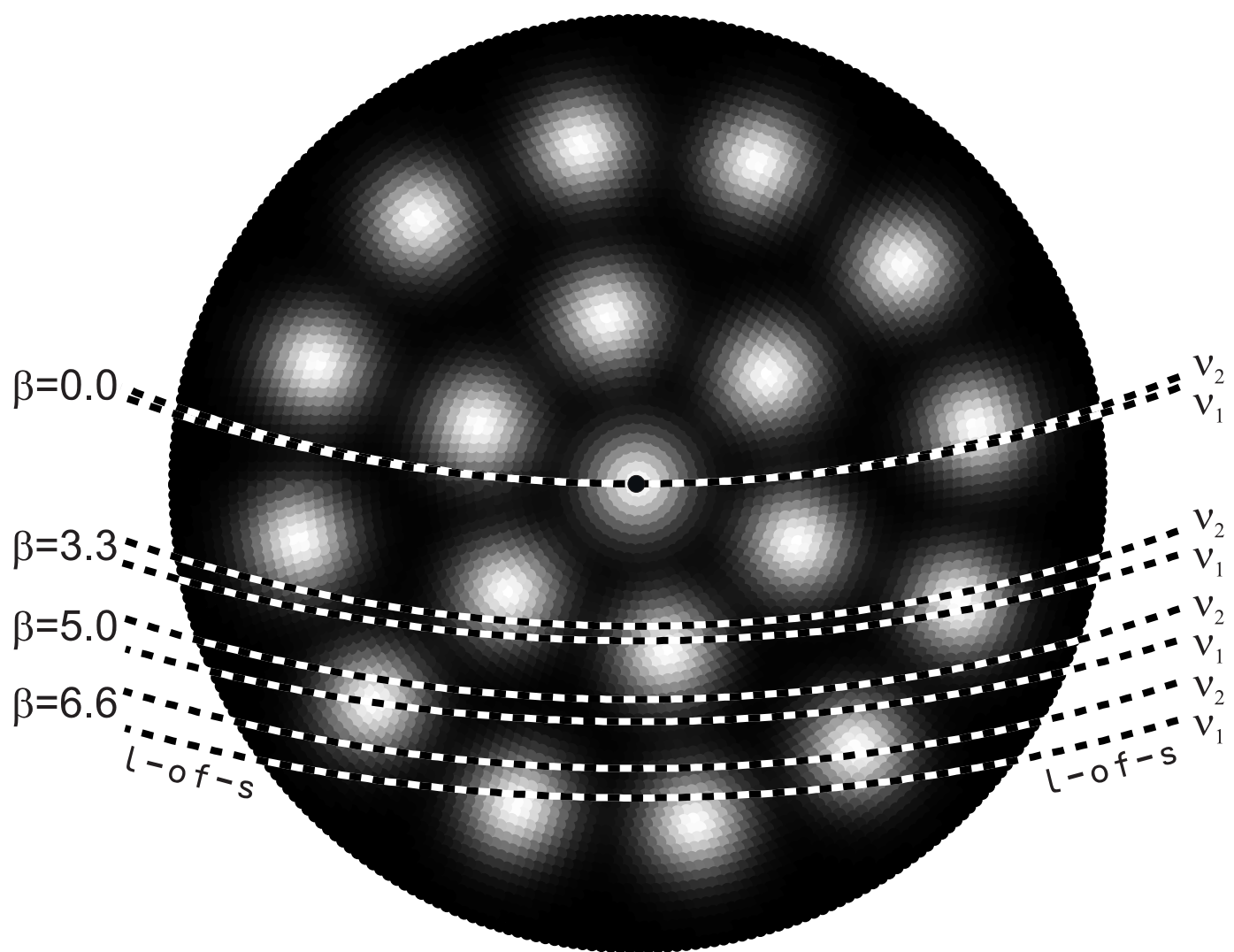




$P=0.7\text{s}$   
 $\alpha=30\text{ deg}$

$\Omega$   
↑

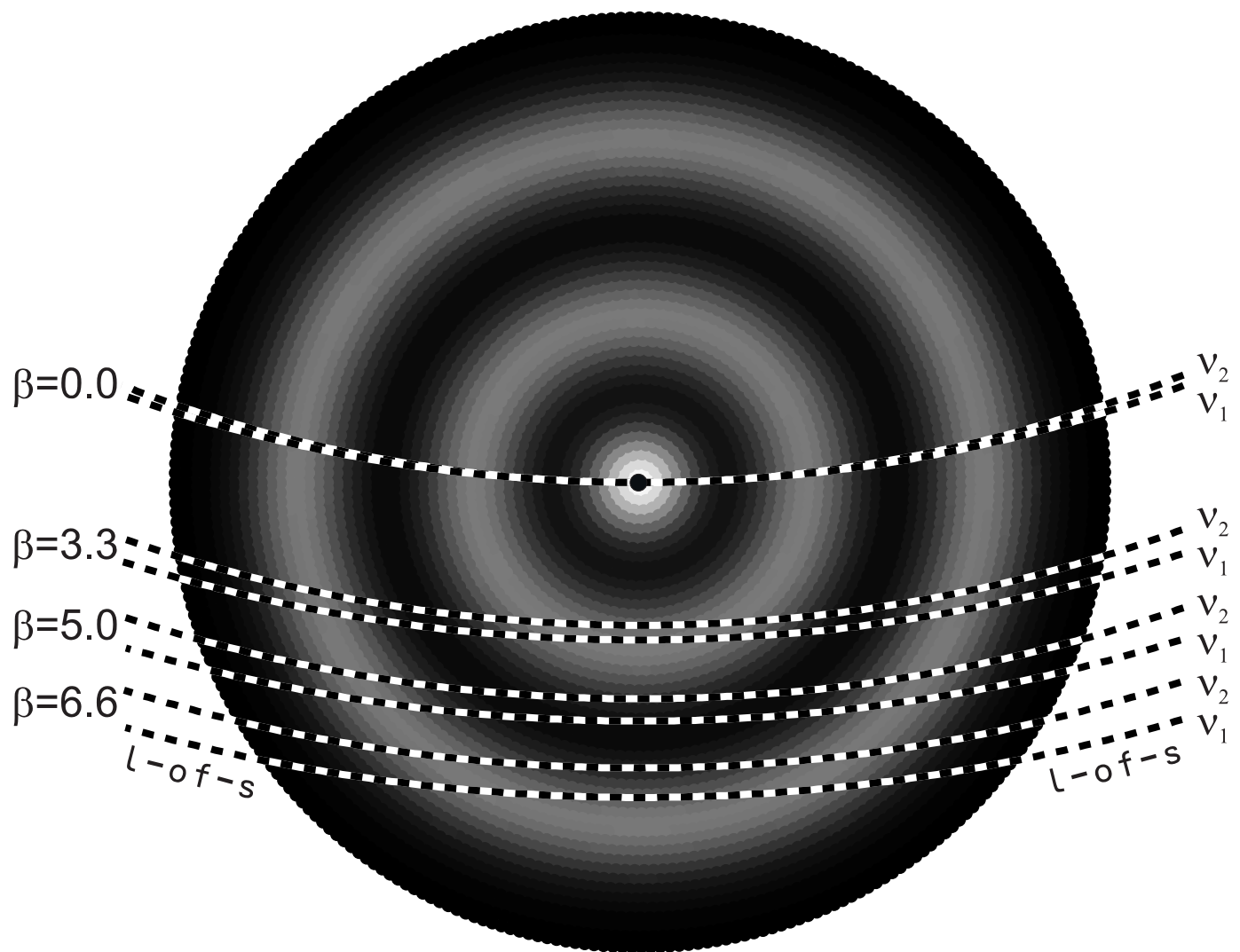
$v_2=238\text{ MHz}$   
 $v_1=610\text{ MHz}$



$P=0.7\text{ s}$   
 $\alpha=30\text{ deg}$

$\Omega$   
↑

$\nu_2=238\text{ MHz}$   
 $\nu_1=610\text{ MHz}$

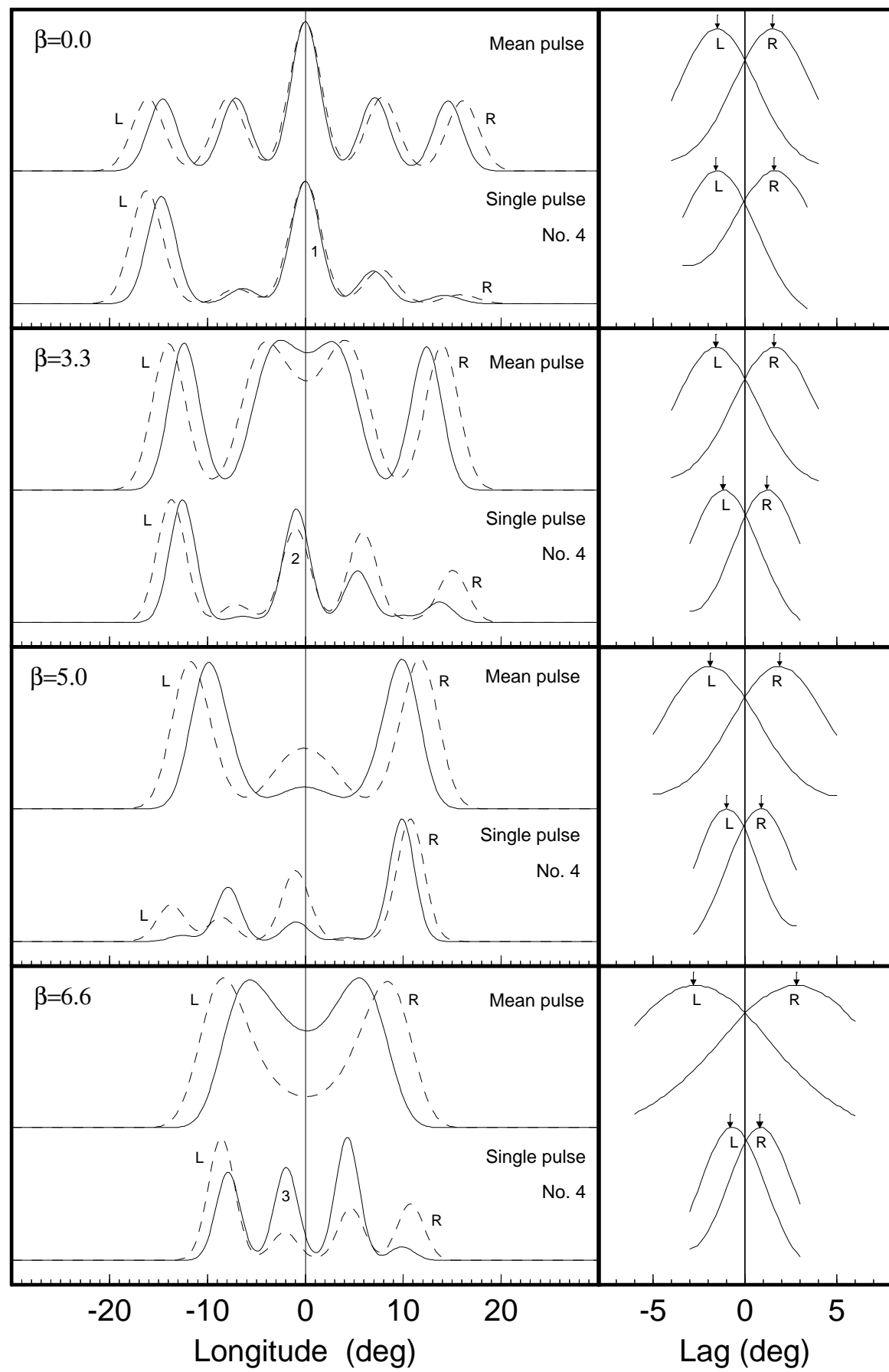


$\alpha=30.0$  deg

--- 238 MHz

— 610 MHz

CCF



CCF

